ACS APPLIED MATERIALS & INTERFACES

www.acsami.org

Research Article

Synergy of Surface Phosphates and Oxygen Vacancies Enables Efficient Photocatalytic Methane Conversion at Room Temperature

Xin-Ke Zhou, Yu Li,* Pei-Pei Luo, and Tong-Bu Lu*

Cite This: *ACS Appl. Mater. Interfaces* 2023, 15, 36280−36288

Read Online

ACCESS | Metrics & More | Article Recommendations | Supporting Information

Downloaded via TIANJIN UNIV OF TECHNOLOGY on September 1, 2023 at 07:16:24 (UTC).
See https://pubs.acs.org/sharingguidelines for options on how to legitimately share published articles.

ABSTRACT: Room-temperature photocatalytic conversion of CH_4 into liquid oxygenates with O_2/H_2O provides an appealing route for sustainable chemical industry, which, however, suffers from poor efficiency due to the undesired carrier kinetics and low yield of reactive oxygen species of the currently available photocatalysts. Here, we report an effective surface engineering strategy where concurrent constructions of oxygen vacancies and phosphate sites on TiO_2 nanosheets address the above challenge. The surface oxygen vacancies and phosphates are respective acceptors of photogenerated electrons and holes for promoted separation and migration of charge carriers. Moreover, in addition to the facilitated activation of O_2 to $^{\bullet}OH$ by electrons at oxygen vacancies, the surface phosphates also facilely adsorb H_2O via hydrogen bonds and thus effectively transfer holes to H_2O for enhanced $^{\bullet}OH$ production, thereby boosting CH_4 conversion. As a result, compared with TiO_2 sheets with only oxygen vacancies, a 2.8 times improvement in liquid oxygenate production with near-unity selectivity is achieved by virtue of the synergy of surface oxygen vacancies and phosphate sites, together with an unprecedent quantum efficiency of 19.8% under 365 nm irradiation.

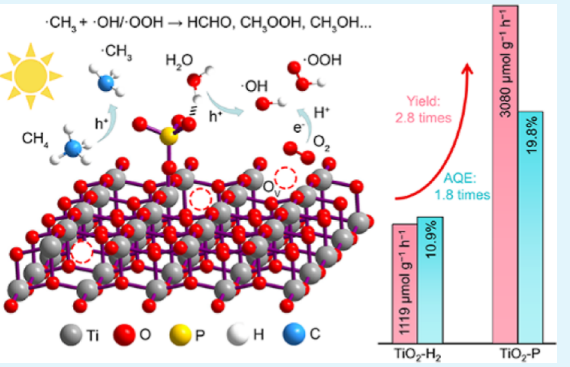

KEYWORDS: *photocatalytic CH_4 conversion, oxygen vacancy, phosphate, O_2 reduction, H_2O oxidation*

1. INTRODUCTION

As a crucial fossil fuel and industrial feedstock, CH_4 is widely distributed in natural gas, shale gas, methane hydrate, and other substances.[1−3] In addition, methane is also one of the main greenhouse gases. Thus, converting methane into value-added liquid chemicals is of both economic and environmental value.[4,5] Unfortunately, the highly symmetric molecule structure makes the activation of C−H bonds extremely difficult. In traditional craft, the conversion of methane usually requires harsh conditions such as high temperature, high pressure, and a strong oxidant, leading to enormous energy consumption and CO_2 emmision.[6,7] It has been deemed as the "holy grail" in catalysis to efficiently convert methane under mild conditions.

Renewable solar energy-driven conversion of CH_4 into liquid oxygenates with O_2 in aqueous conditions holds a great potential in tackling the above challenge.[8−14] Substituting cheap O_2 or H_2O for expensive oxidants like H_2O_2 significantly increases the economic viability of photocatalytic CH_4 conversion.[15−17] However, albeit exciting progresses have been made in this field, there still exist tough issues including a low CH_4 conversion rate and poor selectivity for target products. Moreover, it has been recognized that reactive oxygen species (ROS) plays a vital role in aerobic CH_4 conversion as they may combine with $^{\bullet}CH_3$ or other intermediates to influence the product distribution. To regulate the formation of ROS, noble metal cocatalysts such as Au, Ag, and Pd are usually introduced in semiconductors, which results in elevated cost.[18−21] Our previous work has demonstrated that surface oxygen vacancies can serve as both active sites for O_2 adsorption and effective acceptor for photogenerated electrons, therefore promoting the activation of O_2 to $^{\bullet}OH$ for selective HCHO production from CH_4.[22] Despite the avoidance of metal cocatalysts, the utilization of incident light still needs further improvement considering the apparent quantum efficiency (AQE) value of 7.96% under 360 nm irradiation. On an oxygen vacancy-rich TiO_2 surface, ROS including $^{\bullet}OH$ and $^{\bullet}OOH$ are mainly generated from O_2 reduction by electrons, and holes only take part in the activation of C−H bonds in CH_4. The insoluble CH_4 and sluggish C−H bond cleavage make the consumption rate of holes far below that of electrons. Such mismatch will cause unexpected carrier stack and recombination of electron−hole pairs.[23] Therefore, steering the kinetics of both electrons and

Received: May 9, 2023
Accepted: July 11, 2023
Published: July 19, 2023

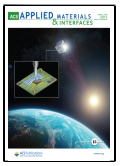

© 2023 American Chemical Society

https://doi.org/10.1021/acsami.3c06376
ACS Appl. Mater. Interfaces 2023, 15, 36280−36288

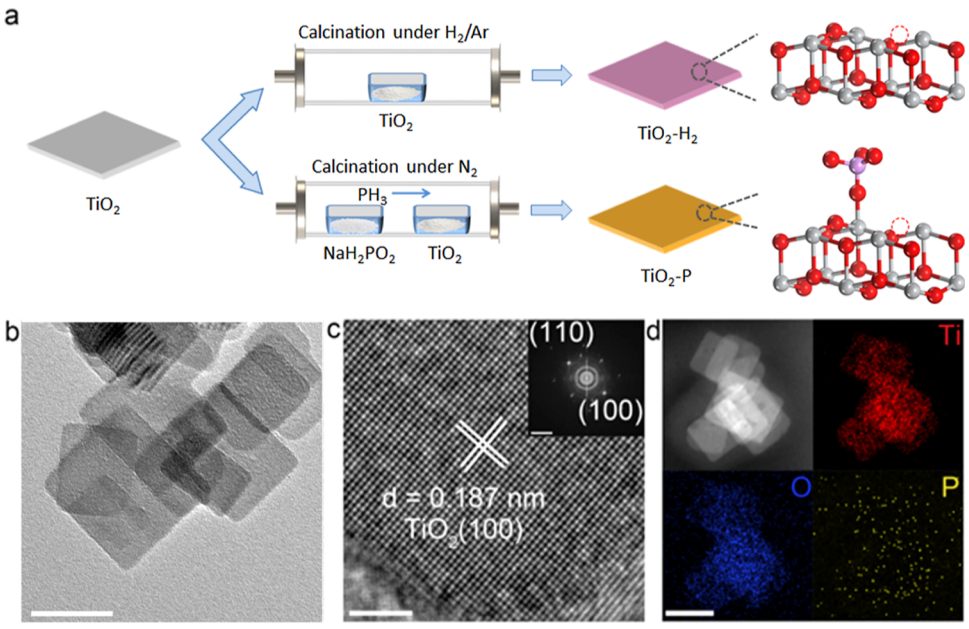

Figure 1. Synthesis and structural characterizations of catalysts. (a) Schematic illustration of the synthesis strategy for TiO_2−H_2 and TiO_2−P. (b) TEM, (c) HRTEM, FFT (inset), and (d) EDS mapping images for TiO_2−P. The scale bars in (b), (c), and (d) are 50, 2, and 50 nm, respectively. The scale bar in the inset of (c) is 5 nm^{-1}.

holes with high ROS yields holds the potential in further enhancing the quantum efficiency of aerobic CH_4 conversion.

Noting that $^{\bullet}OH$ can be produced via O_2 reduction or H_2O oxidation, we herein develop a surface co-modification strategy where concurrent fabrication of surface oxygen vacancies and phosphate sites on TiO_2 nanosheets enables simultaneous production of $^{\bullet}OH$ from both O_2 reduction and H_2O oxidation toward efficient and selective conversion of CH_4 to liquid oxygenates. In situ characterizations reveal that the oxygen vacancies are active sites for O_2 activation to $^{\bullet}OH$ and $^{\bullet}OOH$ with electrons; meanwhile, the phosphate sites can easily interact with H_2O via hydrogen bonds and thus efficiently transfer holes to H_2O for extra $^{\bullet}OH$ production. By virtue of the synergy of oxygen vacancies and phosphates in both regulating carrier kinetics and enhancing reactant adsorption, an excellent yield of liquid oxygenates up to 3080 μmol g^{-1} h^{-1} is achieved with 94.2% selectivity at room temperature, 2.8 times as high as that of TiO_2 with only oxygen vacancies. Moreover, the AQE value reaches 19.8% under 365 nm irradiation, ranking top among the reported performances.

2. EXPERIMENTAL SECTION

2.1. Materials. Tetra-*n*-butyl titanate [$Ti(OBu)_4$] and ammonium acetate were provided by Aladdin. Anhydrous ethanol, hydrofluoric acid (HF, 40 wt %), and acetic acid were bought from Sinopharm Chemical Reagent. Sodium hydroxide, 5,5-dimethyl-1-pyrroline-*N*-oxide (DMPO), pentane-2,4-dione, and coumarin were purchased from Macklin. All reagents and materials were used without further purification. Ultrapure water (Milli-Q water) with a resistivity of 18.2 MΩ cm^{-1} was used in all experiments.

2.2. Synthesis of Catalysts. TiO_2 nanosheets were prepared according to a previous study.[24] Typically, 3.0 mL of HF was dropped into 25.0 mL of $Ti(OBu)_4$, followed by stirring at room temperature for 2 h. The mixed solution was transferred into a 50 mL Teflon autoclave and maintained at 453 K for 36 h. After that, the white precipitate was collected by centrifugation and washed with ultrapure water and ethanol several times. Then, the obtained sample was dispersed into 0.1 M NaOH solution and stirred for 12 h to remove the adsorbed fluoric ions. Finally, the sample was washed with ultrapure water until the supernatant became neutral and dried in vacuum at 333 K.

Next, NaH_2PO_2 (800 mg) was placed in a tube furnace and the TiO_2 samples were located at the downstream side of NaH_2PO_2 with a distance of 7 cm. The furnace was heated to 573 K at a ramping rate of 10 K min^{-1} and kept for 1 h under N_2 flow. The obtained sample was denoted as TiO_2−P. Control samples were prepared by annealing the prepared TiO_2 nanosheets in O_2 or H_2/Ar at 573 K for 1 h, denoted as TiO_2−O_2 or TiO_2−H_2.

2.3. Characterizations. The powder X-ray diffraction (XRD) patterns were obtained using a Rigaku SmartLab 9 kW X-ray diffractometer with Cu Kα radiation (λ = 1.5418 Å). Transmission electron microscopy (TEM) and high-resolution TEM (HRTEM) were performed on an FEI Tecnai G2 Spirit Twin transmission electron microscope and an FEI Talos F200X transmission electron microscope, respectively. X-ray photoelectron spectroscopy (XPS) analyses were carried out using a Thermo Scientific ESCALAB250Xi spectrometer equipped with monochromatic Al Kα as the excitation source (1486.6 eV). All XPS spectra were corrected with a binding energy of 284.8 eV for C 1s peak. The steady-state photoluminescence (PL) measurements were performed on an F-4600 fluorescence spectrophotometer. Time-resolved PL (TRPL) curves were recorded on a PicoQuant Microtime 200 time-resolved confocal fluorescence instrument. Diffuse reflectance spectroscopy spectra were recorded on a PerkinElmer Lambda 750 UV/Vis/NIR spectrometer. Ultraviolet−visible (UV−vis) spectroscopy measurements were performed on a Hitachi U-3900 UV/vis spectrometer. Nuclear magnetic resonance (NMR) spectra were recorded using a Bruker 400 MHz NMR instrument. The electron paramagnetic resonance (EPR) spectra were recorded using a Bruker EMXplus-6/1 instrument. Raman spectroscopy measurements were conducted on a LabRAM HR Evolution confocal Raman microscope (HORIBA Jobin Yvon, France).

Photoelectrochemical measurements were conducted with a three-electrode system connected to an electrochemical workstation (CHI 760e). A piece of fluorine-doped tin oxide (FTO) glass (1.0 × 1.0 cm^2) uniformly coated with 0.5 mg of the catalyst, platinum foil, and a Ag/AgCl electrode were used as the working electrode, the counter electrode, and the reference electrode, respectively. Na_2SO_4 solution (0.1 M) was employed as the electrolyte. A 300 W Xe lamp (CEL-HXF300, CEAULIGHT) was used as the light source.

https://doi.org/10.1021/acsami.3c06376
ACS Appl. Mater. Interfaces 2023, 15, 36280−36288

2.4. Photocatalytic CH_4 Conversion. Photocatalytic methane conversion was carried out in a 50 mL high-pressure reactor which allows overhead irradiation. A 300 W Xenon lamp (CEL-HXF300, CEAULIGHT) with a UV light intensity of 50 mW cm^{-2} was fixed over the high-pressure reaction as the light source. The catalyst (5 mg) was well-dispersed in water (10 mL) through sonication for 30 min, and the mixture was then transferred into the reactor. The sealed reactor was first purged with Ar for 1 h and filled with O_2/CH_4 mixed gas with a total pressure of 2.0 MPa. After illumination for certain time at 298 K, the reactor was cooled down in an ice−water bath before collecting the products.

2.5. Product Analysis. The gas products were detected using gas chromatography (GC). CO_2 was analyzed using an Agilent 7820A gas chromatograph equipped with a HP-PLOT/Q column connected to a thermal conductivity detector. Other gas products were detected using a Shimadzu GC-2014 gas chromatograph equipped with one MolSieve 5A, two Porapak N, and one Porapak Q columns. In addition, two flame ionization detectors and one thermal conductivity detector were employed. CH_3OH, CH_3OOH, and HCOOH were quantified using ^1H NMR with water suppression. The ^{13}C-labeling isotope experiment was conducted under a $^{13}CH_4$ atmosphere, and the produced HCHO was detected using C NMR. The amounts of HCHO were determined through a colorimetric method.[25−27]

2.6. Analysis of Radicals. DMPO was used as the spin-trapping agent to detect the $^{\bullet}OOH$ and $^{\bullet}OH$ radicals.[28] For the detection of $^{\bullet}OH$, an aqueous suspension (2 mg of catalyst in 500 μL of H_2O) was mixed with 40 μL of DMPO in a O_2 or an Ar atmosphere. After the mixture being illuminated for 10 min, the EPR spectra was collected. $^{\bullet}OOH$ was detected by a similar method except that the catalyst and DMPO were dispersed in O_2-saturated methanol. In addition, the production of $^{\bullet}OH$ was further determined using coumarin as a probe molecule via monitoring the PL peak at 412 nm corresponding to 7-hydroxycoumarin, which is specifically formed by the combination of coumarin and $^{\bullet}OH$.[29−31] Specifically, the catalyst (2 mg) was dispersed in a coumarin aqueous solution (2 mM, 2 mL). The mixture was purged by O_2 for 30 min and irradiated using a 300 W Xe lamp with a UV filter for 30 min. To determine the $^{\bullet}OH$ production from water oxidation, 30 mM $NaIO_3$ was added as electron-acceptor, and the mixture was purged by Ar.

2.7. In Situ Raman Spectroscopy Measurements. In situ Raman spectroscopy measurements were performed using a LabRAM HR Evolution Confocal Raman microscope equipped with an aberration-corrected Czerny Turner total reflection spectrometer with a focal length of 800 nm (HORIBA JY). A 532 nm laser was employed as the excitation source, and the Raman system was calibrated using a neon lamp (585 nm). The Raman spectra were recorded by averaging five scans at 1800 gr/mm with an acquisition time of 10 s after various irradiation times. In a gas-tight Teflon cell filled with H_2O vapor and CH_4, a piece of FTO glass loaded with 0.5 mg cm^{-2} catalyst was placed perpendicular to the lens.

3. RESULTS AND DISCUSSION

3.1. Structural Characterizations of the Catalyst. Schematic illustration for the synthesis of TiO_2−H_2 and TiO_2−P is shown in Figure 1a. The reductive PH_3 from NaH_2PO_2 decomposition extracted the surface lattice oxygen from TiO_2 nanosheets, forming oxygen vacancies and phosphate near the coordinatively unsaturated Ti sites.[32,33] The XRD patterns in Figure S1 showed only the typical anatase phase (JCPDS #21-1272) for all the three TiO_2 samples, indicating no phase transition after the heat treatments. To further disclose the morphology and facet structure for the catalysts, HRTEM characterization was carried out. Rectangular nanosheets with sizes ranging from 40 to 60 nm were observed for TiO_2−P (Figure 1b). As shown in Figure 1c, orthogonal lattice fringes with an interplanar spacing of 0.187 nm corresponding to {100} planes demonstrate the mainly exposed (001) facet for TiO_2−P nanosheets, which was also confirmed by the fast Fourier transform image (inset in Figure 1c). Similar structures were also observed for TiO_2−O_2 and TiO_2−H_2 (Figure S2). Energy-dispersive spectroscopic (EDS) mapping in Figure 1d suggests the uniform distribution of P species over TiO_2 nanosheets for TiO_2−P.

EPR measurement was performed to determine the concentration of oxygen vacancies in different catalysts. As shown in Figure 2a, TiO_2−H_2 and TiO_2−P both display strong

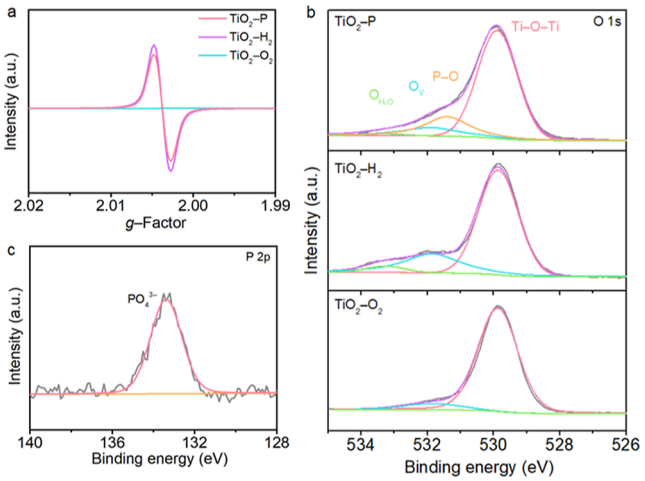

Figure 2. Characterization of oxygen vacancies and P species. (a) EPR, (b) O 1s XPS, and (c) P 2p XPS spectra for TiO_2−O_2, TiO_2−H_2, and TiO_2−P.

signals centered at g = 2.002 due to the single electron trapped by oxygen vacancies, indicative of the successful creation of oxygen vacancies in these two catalysts.[34,35] The oxygen vacancy concentration of TiO_2−H_2 is slightly higher than that of TiO_2−P. On the contrary, no signal appeared in the EPR spectrum of TiO_2−O_2, demonstrating the thorough removal of possible oxygen vacancies by O_2 treatment.

To further explore the surface structure and chemical states, surface-sensitive characterizations including Raman and XPS measurements were conducted. As depicted in Figure S3a, the six first-order Raman-active vibrations ($3E_g$ + $2B_{1g}$ + A_{1g}) assigned to only anatase TiO_2 were clearly observed for the catalysts.[34,36] Notably, the strongest peak of E_g symmetry Ti−O stretching in TiO_2−P blue-shifts gradually from 143.4 to 144.5 cm^{-1} compared to that of TiO_2−O_2 (Figure S3b), which can be attributed to the lattice disorder induced by the surface defects and coordination with P species.[18] Figure 2b shows the O 1s XPS spectra for these samples. The O 1s region of TiO_2−P can be reasonably deconvoluted into four peaks at 529.9, 531.4, 531.9, and 533.3 eV, belonging to the lattice oxygen (Ti−O−Ti), P−O species, oxygen vacancies, and physically adsorbed H_2O, respectively, indicating the presence of both surface oxygen vacancies and phosphate-like species over TiO_2−P.[37−40] The chemical state of P species was further verified by P 2p XPS spectrum of TiO_2−P, where a single peak with a binding energy of 133.4 eV attributed to PO_4^{3-} was observed. To further confirm the surface phosphate sites for TiO_2−P, P 2p XPS spectrum after Ar plasma etching was recorded. As shown in Figure S4, the peak intensity of PO_4^{3-} decreased drastically after Ar plasma etching, evidencing that the phosphate sites mainly existed on TiO_2 surface rather than

https://doi.org/10.1021/acsami.3c06376
ACS Appl. Mater. Interfaces 2023, 15, 36280−36288

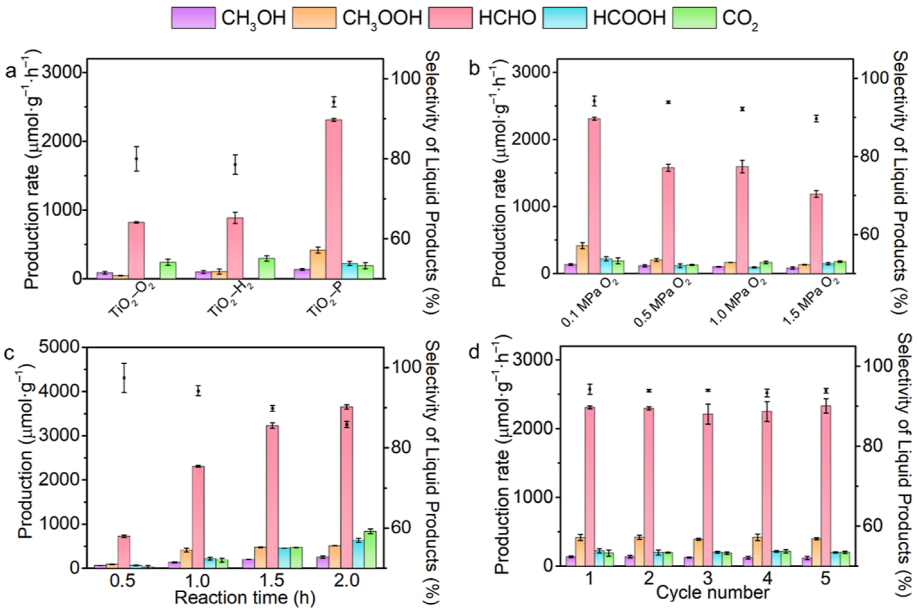

Figure 3. Photocatalytic methane conversion performances. (a) Yields of various products and total selectivity of liquid products for TiO_2−O_2, TiO_2−H_2, and TiO_2−P. (b) Effect of O_2 partial pressure on photocatalytic CH_4 conversion over TiO_2−P. (c) Time-dependent photocatalytic performance for TiO_2−P. (d) Stability test of five consecutive cycles for TiO_2−P.

doped in the bulk lattice. The result of FT-IR spectra also confirms the presence of phosphate species on TiO_2−P (Figure S5). The strong bands at 3448 and 1647 cm^{-1} can be due to the surface hydroxyl groups.[41,42] The enlarged spectrum for TiO_2−P clearly displays two bands located at 1127 and 1020 cm^{-1} that are assigned to the symmetric stretching vibration of O−P−O and P−O bonds in PO_4^{3-}, respectively.[41−43]

3.2. Photocatalytic CH_4 Conversion Performances. Upon acquiring the structure of these catalysts, we are going to evaluate the efficacy of surface oxygen vacancies and phosphates in photocatalytic methane conversion. The photocatalytic performances were first assessed in a top-irradiation high-pressure batch reactor filled with 1.9 MPa CH_4 and 0.1 MPa O_2 at room temperature and the results are listed in Table S1.[22] As shown in Figure 3a, HCHO is the main product for all catalysts, and neither CO nor H_2 was detected in the gas product. Specifically, TiO_2−O_2 only delivers a HCHO production rate of 819 μmol g^{-1} h^{-1} with a liquid product selectivity of 79.9%. Surface oxygen vacancies endow TiO_2−H_2 with an increased HCHO production rate of 917 μmol g^{-1} h^{-1}, whereas the liquid product selectivity is still around 80% due to the overoxidation of CH_4 to CO_2. In sharp contrast, for TiO_2−P, the introduction of surface phosphate markedly boosts the production rate of HCHO up to 2309 μmol g^{-1} h^{-1}, 2.8 and 2.5 times higher than those of TiO_2−O_2 and TiO_2−H_2, respectively. Meanwhile, a total production rate of liquid products up to 3080 μmol g^{-1} h^{-1} was achieved with a high selectivity of 94.2%. It proves that the surface phosphate can not only facilitate the conversion of methane but also suppress the overoxidation of methane to CO_2. The AQEs under different wavelengths of incident light were determined (Figure S6). An impressive AQE value of up to 19.8% was achieved by TiO_2−P under a 365 nm incident light. Such a high production rate and selectivity of liquid products and AQE for TiO_2−P rank top-level among the performances of reported photocatalytic methane conversion systems (Table S2).

We further investigated the influence of the partial pressure of CH_4 and O_2 on the photocatalytic performance of TiO_2−P (Figure 3b). The total pressure was kept at 2.0 MPa. The CH_4 conversion rate decreases as the O_2 partial pressure increases, which can be attributed to the reduced amount of dissolved CH_4. Conversely, the selectivity of CO_2 increases, signifying that excessive O_2 will result in further oxidation of liquid products.[26,30] The effect of total pressure on catalyst performance was evaluated at the optimized ratio of CH_4/O_2 = 19:1(Figure S7). The HCHO production rate was boosted from 2309 to 3581 μmol g^{-1} h^{-1} when the total pressure was increased from 2.0 to 3.0 MPa. However, further increasing the total pressure to 4.0 MPa only contributed to a slightly increased HCHO production rate of 3966 μmol g^{-1} h^{-1}, indicating that the pressure effect on the performance of CH_4 oxidation becomes weaker under higher pressure conditions. We have also assessed the photocatalytic performances with different amounts of water. As revealed by Figure S8, the HCHO production rate gradually increases as the amount of water increases, with the liquid product selectivity kept over 90%, suggesting that the increased amount of water is beneficial to photocatalytic CH_4 conversion. Time-dependent photocatalytic experiments (Figure 3c) reveal that as the reaction time was prolonged from 0.5 to 2 h, the total product yield increases from 977 to 5890 μmol g^{-1}. Meanwhile, deeper oxidation products beyond HCHO, i.e., HCOOH and CO_2, increase, which can be ascribed to the oxidation of accumulated primary products with a higher concentration. As a result, the selectivity of liquid products decreases slightly from 98.3 to 85.8%.

The stability of TiO_2−P was also examined. During five consecutive cyclic tests, neither the production rate nor the liquid product selectivity displays distinguishable decrease (Figure 3d). Characterizations for the catalyst after long-term tests were further conducted (Figure S9). TiO_2−P maintained its rectangular nanosheet structure after reactions. In addition, EPR, XPS, and FT-IR results reveal that the oxygen vacancy and surface phosphates are both well maintained. These results

https://doi.org/10.1021/acsami.3c06376
ACS Appl. Mater. Interfaces 2023, 15, 36280−36288

confirm the exceptional stability of TiO_2−P in photocatalytic methane conversion.

Possible surface carbon contaminant may influence the performance of photocatalytic methane conversion. To testify the origin of C in the product, ^{13}C-labeling isotope experiment was performed with $^{13}CH_4$. As revealed by the ^{13}C NMR spectra (Figure S10), the peaks at 64.9 and 81.8 ppm are attributed to $^{13}CH_3OOH$ and $HO^{13}CH_2OH$ (hydrated $H^{13}CHO$), respectively, proving that the photocatalytic products are derived from CH_4.[28] This is also verified by the control experiments where no product is detected in the absence of CH_4 (Table S3).

3.3. Insights into Photogenerated Charge Carrier Dynamics. To unveil the role of surface phosphates and oxygen vacancies in enhancing the photocatalytic CH_4 conversion, we first investigated the photogenerated charge carrier dynamics over different catalysts. The energy band structures of the catalysts were disclosed using UV−vis diffuse reflectance spectroscopy and Mott−Schottky tests.[44] As revealed in Figure S11, all catalysts show strong light absorption in the sub-400 nm region. Besides, the absorption edges of TiO_2−H_2 and TiO_2−P both extend to the visible light region compared with TiO_2−O_2, which might be attributed to the new energy levels created by oxygen vacancies and coordinated phosphates.[45,46] According to the Kubelka−Munk equation, the band gap energies were calculated to be 3.12, 2.93, and 3.05 eV for TiO_2−O_2, TiO_2−H_2, and TiO_2−P, respectively. The positive slopes of the Mott−Schottky plots suggest the n-type semiconductor characteristics of these TiO_2-based catalysts (Figure S12a−c) and thus the conduction band minimum can be estimated using the flat band value.[47,48] The flat bands of TiO_2−O_2, TiO_2−H_2, and TiO_2−P to NHE are −0.33, −0.45, and −0.39 eV, respectively. On the basis of the above results, the energy band diagrams of these catalysts were drawn and are shown in Figure S12d. Notably, the elevated valence band edges will reasonably reduce the oxidation ability of photogenerated holes, which may account for the suppressed overoxidation of CH_4 to CO_2 on TiO_2−H_2 and TiO_2−P.

To gain in-depth understanding about the effect of oxygen vacancies and coordinated phosphates on the kinetics of photogenerated charge carriers, transient photocurrent response test was carried out (Figure 4a). Among the three samples, TiO_2−P delivered the highest photocurrent response, suggesting that surface oxygen vacancies and phosphates effectively promote the separation of photogenerated charge carriers. In addition, the interfacial charge transfer is significantly facilitated by surface oxygen vacancies and phosphates according to the EIS spectra under dark/light circumstances in Figure 4b.[49] As revealed by TRPL measurements (Figure 4c), an average luminescence lifetime of 2.3 ns was achieved by TiO_2−P, longer than that of TiO_2−H_2 (1.4 ns) and TiO_2−O_2 (2.0 ns), indicating that the surface oxygen vacancies and phosphates prolong the charge carrier lifetime.[50] This is further validated by OCVD results, where similar trends in the average lifetime of photogenerated charge carriers were observed for the samples (Figures S13; 4d). Therefore, we can conclude that the surface oxygen vacancies and phosphates can jointly promote the separation and migration of photogenerated charge carriers toward enhanced utilization efficiency of incident light.

3.4. Mechanism of CH_4 Conversion. ROSs play a vital role in aerobic photocatalytic CH_4 conversion, as their types

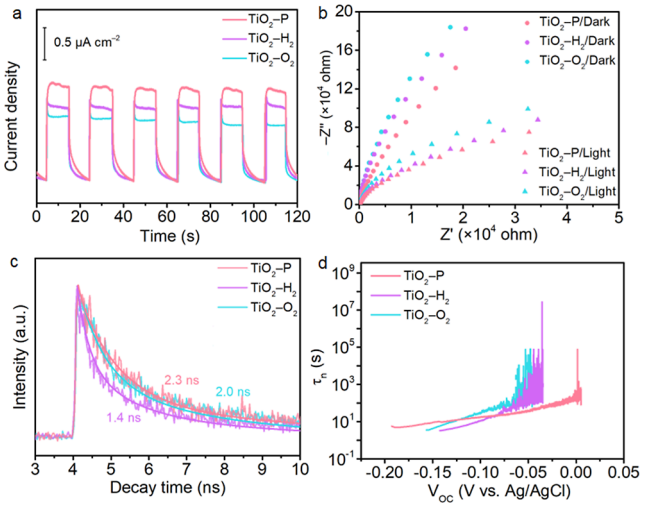

Figure 4. Photogenerated charge carrier kinetic analysis. (a) Transient photocurrent responses, (b) electrochemical impedance spectra under dark/light conditions, (c) TRPL spectra, and (d) transformed OCVD curves for TiO_2−O_2, TiO_2−H_2, and TiO_2−P.

and yields directly affect the selectivity and production rate of products.[51,52] Hence, EPR trapping measurements in an O_2 atmosphere were performed using DMPO as a spintronic trapping agent to detect the generation of ROS under illumination. Figure 5a shows strong signals corresponding to

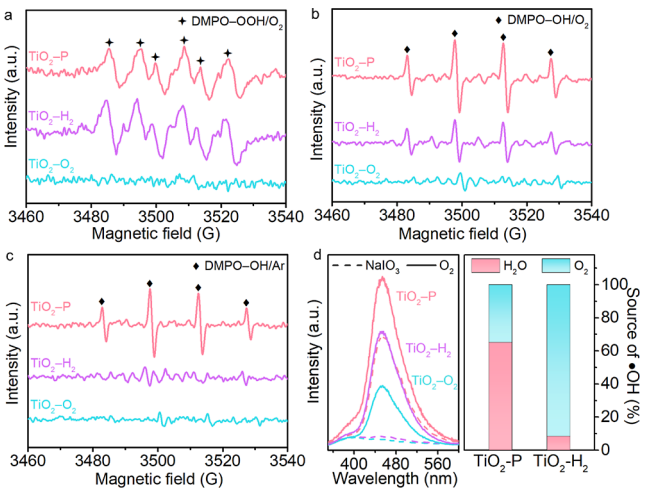

Figure 5. Detection of ROSs. DMPO spin-trapping EPR spectra for (a) $^{\bullet}$OOH and (b) $^{\bullet}$OH in an O_2 atmosphere. (c) DMPO spin-trapping EPR spectra for $^{\bullet}$OH in an Ar atmosphere. (d) Analysis of $^{\bullet}$OH from H_2O/O_2 using coumarin.

DMPO−OOH species for both TiO_2−P and TiO_2−H_2, which accounts for the detection of CH_3OOH in liquid products (Figure 3a). Moreover, TiO_2−P exhibits much higher $^{\bullet}$OH yield compared with TiO_2−H_2 (Figure 5b), which agrees well with the enhanced HCHO production for TiO_2−P. In sharp contrast, TiO_2−O_2 only produces negligible $^{\bullet}$OOH and $^{\bullet}$OH based on the weak EPR signals. Typically, $^{\bullet}$OOH or superoxide anion radical ($^{\bullet}O^{2-}$) can be generated via the reduction of O_2 molecules by photogenerated electrons.[53] This is also confirmed by the EPR result in an Ar atmosphere that no $^{\bullet}$OOH is detected (Figure S14). Of note, $NaIO_3$ was employed as an electron acceptor during the test to minimize

https://doi.org/10.1021/acsami.3c06376
ACS Appl. Mater. Interfaces 2023, 15, 36280−36288

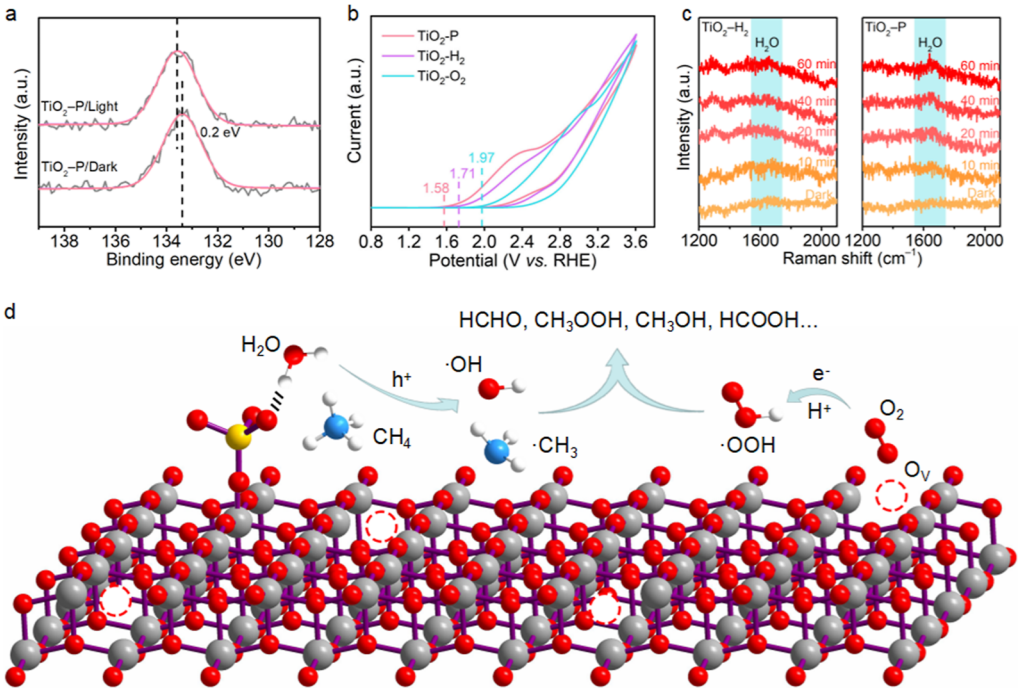

Figure 6. Mechanism study on the enhanced photocatalytic performance. (a) In situ P 2p XPS spectra of TiO_2−P under darkness/light irradiation. (b) CV curves of TiO_2−O_2, TiO_2−H_2, and TiO_2−P in O_2-saturated 0.1 M Na_3PO_4. (c) In situ Raman spectra for TiO_2−H_2 and TiO_2−P in the presence of H_2O. (d) Schematic illustration of the reaction mechanism for the photocatalytic conversion of CH_4. The gray, red, blue, yellow, and white spheres represent Ti, O, C, P, and H atoms, respectively, and the dashed circles represent oxygen vacancies.

the stack effect of photogenerated electrons in an Ar atmosphere. However, •OH can be produced via the reduction of O_2 by electrons or oxidation of H_2O by holes.[53] Our previous work has demonstrated that •OH mainly comes from O_2 reduction on defective TiO_2 nanosheets.[22] As expected, barely no signal related to DMPO−OH emerges on TiO_2−H_2 in an Ar atmosphere (Figure 5c). Interestingly, strong DMPO−OH peaks were observed for TiO_2−P in the absence of O_2, implying that a large proportion of •OH origins from water oxidation. This result also explains that a certain amount of CH_3OH was detected during the photocatalytic methane conversion in the absence of O_2 (Table S3). Therefore, we can deduce that •OOH radicals generated mainly from the reduction of O_2, whereas •OH radicals come from both reduction of O_2 and oxidation of H_2O.

As a step further, coumarin was employed as a probe to determine the ratio of •OH from H_2O/O_2 (Figure 5d). The intensity of the PL peak at 412 nm is proportional to the •OH concentration. Clearly, the PL peak intensities in an O_2 atmosphere follows the trend of TiO_2−P > TiO_2−H_2 > TiO_2−O_2, consistent with the EPR results in Figure 5b. Notably, only TiO_2−P displays a strong PL peak (red dashed line). As a result, a majority of •OH (65%) comes from H_2O for TiO_2−P, whereas 92% of •OH is generated from O_2 by TiO_2−H_2. Therefore, we infer that the phosphates can interact with H_2O molecules via hydrogen bonds and thus efficiently transfer the photogenerated holes to the adsorbed H_2O for enhanced •OH generation.[54]

To verify the above inference, XPS measurement of TiO_2−P under darkness/illumination was first conducted (Figure 6a). The P 2p peak shifts to higher binding energy by 0.2 eV under incident light, demonstrating that phosphates become positively charged owing to the acceptance of photogenerated holes. In addition, water contact angle measurement reveals that surface phosphates make the TiO_2 surface much more hydrophilic compared with TiO_2−O_2 and TiO_2−H_2, indicating the favored H_2O adsorption on TiO_2−P (Figure S15).

To further evaluate the enhanced H_2O dissociation on phosphate sites, cyclic voltammetry (CV) measurements were carried out in O_2-saturated 0.1 M Na_3PO_4 solution. As displayed by the CV curves in Figure 6b, the onset potential of H_2O oxidation on TiO_2−P is 1.58 V vs the reversible hydrogen electrode, 130 and 390 mV lower than that of TiO_2−H_2 and TiO_2−O_2, respectively, demonstrating the reduced energy barrier of water activation on phosphate sites of TiO_2−P. In situ Raman spectroscopic measurements were also conducted to monitor the H_2O adsorption intermediate on TiO_2−P and TiO_2−H_2 (Figure 6c). No peaks were observed in dark condition for the two catalysts. With the light on, a peak at 1640 cm^{-1} that is assigned to the H−O−H bending vibration appeared on TiO_2−P, and the peak intensity increased with the prolongation of illumination time.[55,56] For comparison, a rather weak adsorbed H_2O peak was observed on TiO_2−H_2, suggesting the poor H_2O adsorption capacity on defective TiO_2 in the absence of surface phosphate. According to the above results, we can reach a conclusion that surface phosphates act as an effective bridge between the photogenerated holes and adsorbed H_2O, thereby promoting H_2O oxidation to •OH radicals for enhanced photocatalytic methane conversion.

The mechanism of C−H bond activation on TiO_2−P was subsequently investigated. As shown in Figure S16, only trace amounts of CH_3OH and HCHO were produced with the addition of Fenton reagent, signifying that the activation of the C−H bond is initiated by photogenerated holes rather than •OH.[57−59] To further confirm this deduction, the performance of photocatalytic methane conversion was assessed with the addition of Na_2S to annihilate the photogenerated holes

https://doi.org/10.1021/acsami.3c06376
ACS Appl. Mater. Interfaces 2023, 15, 36280−36288

(Figure S17). Consequently, negligible amounts of products were detected, validating the essential role of photogenerated holes in CH_4 activation. In situ Raman spectroscopic measurements in a CH_4 atmosphere were performed to explore the C−H bond activation on catalysts (Figure S18). A peak at 2917 cm^{-1} corresponding to the C−H asymmetric stretching vibration of $*CH_3$ was observed for both TiO_2−H_2 and TiO_2−P under illumination, indicating the cleavage of the first C−H bond in CH_4 on TiO_2 surface.[22] The stronger $*CH_3$ peak for TiO_2−P confirms the enhanced CH_4 activation by virtue of phosphate sites.

Therefore, we reasonably propose a reaction route for the photocatalytic conversion of CH_4 on TiO_2−P (Figure 6d). The photogenerated electrons migrate to the O_2 adsorbed at surface oxygen vacancies for the formation of $^{\bullet}OOH$ ($O_2 + e^- + H^+ \rightarrow {}^{\bullet}OOH$) or $^{\bullet}OH$ ($O_2 + 2e^- + 2H^+ \rightarrow H_2O_2$; $H_2O_2 + e^- \rightarrow {}^{\bullet}OH + OH^-$); meanwhile, the surface phosphates adsorb H_2O via the hydrogen bond and transfer the photogenerated holes to the latter, thus oxidizing H_2O into $^{\bullet}OH$ radicals ($H_2O + h^+ \rightarrow {}^{\bullet}OH + H^+$). The cleavage of the C−H bond in CH_4 is also triggered by photogenerated holes on the catalyst surface ($CH_4 + h^+ \rightarrow {}^{\bullet}CH_3 + H^+$). Finally, $^{\bullet}CH_3$ combines with $^{\bullet}OOH$ or $^{\bullet}OH$ to generate CH_3OOH or CH_3OH, respectively. The formed CH_3OH can be further oxidized into HCHO as indicated by the results in Figure S19 that HCHO was the main product with the addition of CH_3OH in the absence of CH_4.[60]

4. CONCLUSIONS

In conclusion, we have successfully synthesized an efficient photocatalyst featuring TiO_2 nanosheets with surface oxygen vacancies and phosphates for selective aerobic methane conversion at room temperature. In situ DMPO spin-trapping EPR and XPS spectra, as well as charge carrier kinetic analysis revealed that the surface oxygen vacancies and phosphates acted as the acceptors of photogenerated electrons and holes, respectively, thus promoting the separation and migration of photogenerated charge carriers. Moreover, in addition to the enhanced O_2 activation at oxygen vacancies by electrons, facile H_2O adsorption and dissociation were achieved on phosphate sites by holes according to the in situ EPR and Raman spectra, thereby synergistically boosting the ROS production for superior performance of photocatalytic methane conversion. As a result, an impressive quantum efficiency approaching 19.8% was achieved under 365 nm irradiation, and a high production rate for liquid oxygenates up to 3080 μmol g^{-1} h^{-1} was delivered with near-unity selectivity on the TiO_2−P catalyst, 2.8 times as high as that on TiO_2−H_2 with only oxygen vacancies. This work presents a novel strategy toward efficient and selective aerobic methane conversion via building specific active sites enabling simultaneous regulation of photogenerated carriers and enhanced activation of O_2/H_2O and highlights the importance of surface engineering in catalyst design.

■ ASSOCIATED CONTENT

Supporting Information

The Supporting Information is available free of charge at https://pubs.acs.org/doi/10.1021/acsami.3c06376.

XRD patterns, additional TEM images, Raman spectra, FT-IR spectra, AQE values, characterizations of TiO_2−P after the stability test, isotope-labeling experiments, UV−vis diffuse reflectance spectra, Mott−Schottky curves, open-circuit voltage decay curves, additional EPR spectra, water contact angle measurement, additional photocatalytic test, in situ Raman spectra in a CH_4 atmosphere, and comparison of the photocatalytic CH_4 conversion performance of TiO_2−P with those of reported photocatalysts (PDF)

■ AUTHOR INFORMATION

Corresponding Authors

Yu Li − *MOE International Joint Laboratory of Materials Microstructure, Institute for New Energy Materials and Low Carbon Technologies, School of Materials Science & Engineering, Tianjin University of Technology, Tianjin 300384, China;* orcid.org/0000-0003-3691-0199; Email: yli@email.tjut.edu.cn

Tong-Bu Lu − *MOE International Joint Laboratory of Materials Microstructure, Institute for New Energy Materials and Low Carbon Technologies, School of Materials Science & Engineering, Tianjin University of Technology, Tianjin 300384, China;* orcid.org/0000-0002-6087-4880; Email: lutongbu@tjut.edu.cn

Authors

Xin-Ke Zhou − *MOE International Joint Laboratory of Materials Microstructure, Institute for New Energy Materials and Low Carbon Technologies, School of Materials Science & Engineering, Tianjin University of Technology, Tianjin 300384, China*

Pei-Pei Luo − *MOE International Joint Laboratory of Materials Microstructure, Institute for New Energy Materials and Low Carbon Technologies, School of Materials Science & Engineering, Tianjin University of Technology, Tianjin 300384, China*

Complete contact information is available at: https://pubs.acs.org/10.1021/acsami.3c06376

Author Contributions

Conceptualization, Y.L.; methodology, X.Z. and Y.L.; validation, P.L.; formal analysis, Y.L., P.L., and X.Z.; investigation, X.Z. and Y.L.; writing—original draft, Y.L. and X.Z.; writing—review and editing, Y.L.; supervision, T.L.; and funding acquisition, Y.L. and T.L. All authors have given approval to the final version of the manuscript.

Notes

The authors declare no competing financial interest.

■ ACKNOWLEDGMENTS

This work was supported by the National Key R&D Program of China (2017YFA0700104), the National Natural Science Foundation of China (21905204 and 21931007), and 111 Project of China (D17003).

■ REFERENCES

(1) McFarland, E. Unconventional Chemistry for Unconventional Natural Gas. *Science* **2012**, *338*, 340−342.

(2) Meng, X.; Cui, X.; Rajan, N. P.; Yu, L.; Deng, D.; Bao, X. Direct Methane Conversion under Mild Condition by Thermo-Electro-or Photocatalysis. *Chem* **2019**, *5*, 2296−2325.

(3) Villa, K.; Murcia-López, S.; Andreu, T.; Morante, J. R. Mesoporous WO_3 Photocatalyst for The Partial Oxidation of Methane to Methanol Using Electron Scavengers. *Appl. Catal., B* **2015**, *163*, 150−155.

(4) Meyet, J.; Searles, K.; Newton, M. A.; Wörle, M.; van Bavel, A. P.; Horton, A. D.; van Bokhoven, J. A.; Copéret, C. Monomeric Copper(II) Sites Supported on Alumina Selectively Convert Methane to Methanol. *Angew. Chem., Int. Ed.* **2019**, *58*, 9841−9845.
(5) Schwarz, H. Chemistry with Methane: Concepts Rather than Recipes. *Angew. Chem., Int. Ed.* **2011**, *50*, 10096−10115.
(6) Wang, B.; Albarracín-Suazo, S.; Pagán-Torres, Y.; Nikolla, E. Advances in Methane Conversion Processes. *Catal. Today* **2017**, *285*, 147−158.
(7) Wu, X.; Zhang, Q.; Li, W.; Qiao, B.; Ma, D.; Wang, S. L. Atomic-Scale Pd on 2D Titania Sheets for Selective Oxidation of Methane to Methanol. *ACS Catal.* **2021**, *11*, 14038−14046.
(8) Palmisano, G.; García-López, E.; Marcì, G.; Loddo, V.; Yurdakal, S.; Augugliaro, V.; Palmisano, L. Advances in Selective Conversions by Heterogeneous Photocatalysis. *Chem. Commun.* **2010**, *46*, 7074−7089.
(9) Song, H.; Meng, X.; Wang, Z.-j.; Liu, H.; Ye, J. Solar-Energy-Mediated Methane Conversion. *Joule* **2019**, *3*, 1606−1636.
(10) Zeng, Y.; Liu, H. C.; Wang, J. S.; Wu, X. Y.; Wang, S. L. Synergistic Photocatalysis−Fenton Reaction for Selective Conversion of Methane to Methanol at Room Temperature. *Catal. Sci. Technol.* **2020**, *10*, 2329−2332.
(11) Lin, X.-Y.; Li, J.-Y.; Qi, M.-Y.; Tang, Z.-R.; Xu, Y.-J. Methane Conversion over Artificial Photocatalysts. *Catal. Commun.* **2021**, *159*, 106346.
(12) Qi, M.-Y.; Conte, M.; Anpo, M.; Tang, Z.-R.; Xu, Y.-J. Cooperative Coupling of Oxidative Organic Synthesis and Hydrogen Production over Semiconductor-Based Photocatalysts. *Chem. Rev.* **2021**, *121*, 13051−13085.
(13) Wang, P.; Zhang, X.; Shi, R.; Zhao, J.; Yuan, Z.; Zhang, T. Light-Driven Hydrogen Production from Steam Methane Reforming via Bimetallic PdNi Catalysts Derived from Layered Double Hydroxide Nanosheets. *Energy Fuels* **2022**, *36*, 11627−11635.
(14) Zhu, Z.; Guo, W.; Zhang, Y.; Pan, C.; Xu, J.; Zhu, Y.; Lou, Y. Research Progress on Methane Conversion Coupling Photocatalysis and Thermocatalysis. *Carbon Energy* **2021**, *3*, 519−540.
(15) Cui, X.; Li, H.; Wang, Y.; Hu, Y.; Hua, L.; Li, H.; Han, X.; Liu, Q.; Yang, F.; He, L.; Chen, X.; Li, Q.; Xiao, J.; Deng, D.; Bao, X. Room-Temperature Methane Conversion by Graphene-Confined Single Iron Atoms. *Chem* **2018**, *4*, 1902−1910.
(16) Ravi, M.; Ranocchiari, M.; van Bokhoven, J. A. The Direct Catalytic Oxidation of Methane to Methanol—A Critical Assessment. *Angew. Chem., Int. Ed.* **2017**, *56*, 16464−16483.
(17) Zhao, W.; Shi, Y.; Jiang, Y.; Zhang, X.; Long, C.; An, P.; Zhu, Y.; Shao, S.; Yan, Z.; Li, G.; Tang, Z. Fe-O Clusters Anchored on Nodes of Metal−Organic Frameworks for Direct Methane Oxidation. *Angew. Chem., Int. Ed.* **2021**, *60*, 5811−5815.
(18) Luo, L.; Gong, Z.; Xu, Y.; Ma, J.; Liu, H.; Xing, J.; Tang, J. Binary Au−Cu Reaction Sites Decorated ZnO for Selective Methane Oxidation to C1 Oxygenates with Nearly 100% Selectivity at Room Temperature. *J. Am. Chem. Soc.* **2022**, *144*, 740−750.
(19) Feng, N.; Lin, H.; Song, H.; Yang, L.; Tang, D.; Deng, F.; Ye, J. Efficient and Selective Photocatalytic CH_4 Conversion to CH_3OH with O_2 by Controlling Overoxidation on TiO_2. *Nat. Commun.* **2021**, *12*, 4652.
(20) Luo, L.; Luo, J.; Li, H.; Ren, F.; Zhang, Y.; Liu, A.; Li, W.-X.; Zeng, J. Water Enables Mild Oxidation of Methane to Methanol on Gold Single-Atom Catalysts. *Nat. Commun.* **2021**, *12*, 1218.
(21) Luo, L.; Fu, L.; Liu, H.; Xu, Y.; Xing, J.; Chang, C.-R.; Yang, D.-Y.; Tang, J. Synergy of Pd Atoms and Oxygen Vacancies on In_2O_3 for Methane Conversion under Visible Light. *Nat. Commun.* **2022**, *13*, 2930.
(22) Luo, P.-P.; Zhou, X.-K.; Li, Y.; Lu, T.-B. Simultaneously Accelerating Carrier Transfer and Enhancing O_2/CH_4 Activation via Tailoring the Oxygen-Vacancy-Rich Surface Layer for Cocatalyst-Free Selective Photocatalytic CH_4 Conversion. *ACS Appl. Mater. Interfaces* **2022**, *14*, 21069−21078.
(23) Habisreutinger, S. N.; Schmidt-Mende, L.; Stolarczyk, J. K. Photocatalytic Reduction of CO_2 on TiO_2 and Other Semiconductors. *Angew. Chem., Int. Ed.* **2013**, *52*, 7372−7408.
(24) Long, R.; Li, Y.; Liu, Y.; Chen, S.; Zheng, X.; Gao, C.; He, C.; Chen, N.; Qi, Z.; Song, L.; Jiang, J.; Zhu, J.; Xiong, Y. Isolation of Cu Atoms in Pd Lattice: Forming Highly Selective Sites for Photocatalytic Conversion of CO_2 to CH_4. *J. Am. Chem. Soc.* **2017**, *139*, 4486−4492.
(25) Fan, Y.; Zhou, W.; Qiu, X.; Li, H.; Jiang, Y.; Sun, Z.; Han, D.; Niu, L.; Tang, Z. Selective Photocatalytic Oxidation of Methane by Quantum-Sized Bismuth Vanadate. *Nat. Sustain.* **2021**, *4*, 509−515.
(26) Huang, M.; Zhang, S.; Wu, B.; Wei, Y.; Yu, X.; Gan, Y.; Lin, T.; Yu, F.; Sun, F.; Jiang, Z.; Zhong, L. Selective Photocatalytic Oxidation of Methane to Oxygenates over Cu−W−TiO_2 with Significant Carrier Traps. *ACS Catal.* **2022**, *12*, 9515−9525.
(27) Song, H.; Meng, X.; Wang, S.; Zhou, W.; Song, S.; Kako, T.; Ye, J. Selective Photo-Oxidation of Methane to Methanol with Oxygen over Dual-Cocatalyst-Modified Titanium Dioxide. *ACS Catal.* **2020**, *10*, 14318−14326.
(28) Song, H.; Meng, X.; Wang, S.; Zhou, W.; Wang, X.; Kako, T.; Ye, J. Direct and Selective Photocatalytic Oxidation of CH_4 to Oxygenates with O_2 on Cocatalysts/ZnO at Room Temperature in Water. *J. Am. Chem. Soc.* **2019**, *141*, 20507−20515.
(29) Louit, G.; Foley, S.; Cabillic, J.; Coffigny, H.; Taran, F.; Valleix, A.; Renault, J. P.; Pin, S. The Reaction of Coumarin with The OH Radical Revisited: Hydroxylation Product Analysis Determined by Fluorescence and Chromatography. *Radiat. Phys. Chem.* **2005**, *72*, 119−124.
(30) Okolie, C.; Belhseine, Y. F.; Lyu, Y.; Yung, M. M.; Engelhard, M. H.; Kovarik, L.; Stavitski, E.; Sievers, C. Conversion of Methane into Methanol and Ethanol over Nickel Oxide on Ceria−Zirconia Catalysts in A Single Reactor. *Angew. Chem., Int. Ed.* **2017**, *56*, 13876−13881.
(31) Xiang, Q.; Yu, J.; Wong, P. K. Quantitative Characterization of Hydroxyl Radicals Produced by Various Photocatalysts. *J. Colloid Interface Sci.* **2011**, *357*, 163−167.
(32) Li, Y.; Chen, S.; Xi, D.; Bo, Y.; Long, R.; Wang, C.; Song, L.; Xiong, Y. Scalable Fabrication of Highly Active and Durable Membrane Electrodes toward Water Oxidation. *Small* **2018**, *14*, 1702109.
(33) Li, S.-H.; Qi, M.-Y.; Tang, Z.-R.; Xu, Y.-J. Nanostructured Metal Phosphides: From Controllable Synthesis to Sustainable Catalysis. *Chem. Soc. Rev.* **2021**, *50*, 7539−7586.
(34) Gan, Q.; He, H.; Zhu, Y.; Wang, Z.; Qin, N.; Gu, S.; Li, Z.; Luo, W.; Lu, Z. Defect-Assisted Selective Surface Phosphorus Doping to Enhance Rate Capability of Titanium Dioxide for Sodium Ion Batteries. *ACS Nano* **2019**, *13*, 9247−9258.
(35) Chen, X.; Li, J.-Y.; Tang, Z.-R.; Xu, Y.-J. Surface-Defect-Engineered Photocatalyst for Nitrogen Fixation into Value-Added Chemical Feedstocks. *Catal. Sci. Technol.* **2020**, *10*, 6098−6110.
(36) Zhang, J.; Li, M.; Feng, Z.; Chen, J.; Li, C. Uv Raman Spectroscopic Study on TiO_2. I. Phase Transformation at The Surface and in The Bulk. *J. Phys. Chem. B* **2006**, *110*, 927−935.
(37) Cao, M.; Tao, L.; Lv, X.; Bu, Y.; Li, M.; Yin, H.; Zhu, M.; Zhong, Z.; Shen, Y.; Wang, M. Phosphorus-Doped TiO_2-B Nanowire Arrays Boosting Robust Pseudocapacitive Properties for Lithium Storage. *J. Power Sources* **2018**, *396*, 327−334.
(38) Gao, H.; Hu, G.; Sui, J.; Mu, C.; Shangguan, W.; Kong, M.; Shentu, W. Scalable Preparation of Defect-Rich Free-Standing TiO_2 Sheets with Visible-Light Photocatalytic Activity. *Appl. Catal., B* **2018**, *226*, 337−345.
(39) Geng, Z.; Kong, X.; Chen, W.; Su, H.; Liu, Y.; Cai, F.; Wang, G.; Zeng, J. Oxygen Vacancies in ZnO Nanosheets Enhance CO_2 Electrochemical Reduction to CO. *Angew. Chem., Int. Ed.* **2018**, *57*, 6054−6059.
(40) Huo, J.; Xue, Y.; Wang, X.; Liu, Y.; Zhang, L.; Guo, S. TiO_2/Carbon Nanofibers Doped with Phosphorus as Anodes for Hybrid Li-Ion Capacitors. *J. Power Sources* **2020**, *473*, 228551.

https://doi.org/10.1021/acsami.3c06376
ACS Appl. Mater. Interfaces 2023, 15, 36280−36288

(41) Wu, X.; Wu, W.; Liu, C.; Li, S.; Liao, S.; Cai, J. Synthesis of Layered Sodium Manganese Phosphate via Low-Heating Solid State Reaction and Its Properties. *Chin. J. Chem.* **2010**, *28*, 2394−2398.
(42) Yu, J. C.; Zhang, L.; Zheng, Z.; Zhao, J. Synthesis and Characterization of Phosphated Mesoporous Titanium Dioxide with High Photocatalytic Activity. *Chem. Mater.* **2003**, *15*, 2280−2286.
(43) Jing, L.; Zhou, J.; Durrant, J. R.; Tang, J.; Liu, D.; Fu, H. Dynamics of Photogenerated Charges in The Phosphate Modified TiO_2 and The Enhanced Activity for Photoelectrochemical Water Splitting. *Energy Environ. Sci.* **2012**, *5*, 6552−6558.
(44) Zhou, W.; Sun, F.; Pan, K.; Tian, G.; Jiang, B.; Ren, Z.; Tian, C.; Fu, H. Well-Ordered Large-Pore Mesoporous Anatase TiO_2 with Remarkably High Thermal Stability and Improved Crystallinity: Preparation, Characterization, and Photocatalytic Performance. *Adv. Funct. Mater.* **2011**, *21*, 1922−1930.
(45) Zhao, Y.; Zhao, Y.; Shi, R.; Wang, B.; Waterhouse, G. I. N.; Wu, L.-Z.; Tung, C.-H.; Zhang, T. Tuning Oxygen Vacancies in Ultrathin TiO_2 Nanosheets to Boost Photocatalytic Nitrogen Fixation Up to 700 nm. *Adv. Mater.* **2019**, *31*, 1806482.
(46) Zhu, M.; Kim, S.; Mao, L.; Fujitsuka, M.; Zhang, J.; Wang, X.; Majima, T. Metal-Free Photocatalyst for H_2 Evolution in Visible to near-Infrared Region: Black Phosphorus/Graphitic Carbon Nitride. *J. Am. Chem. Soc.* **2017**, *139*, 13234−13242.
(47) Peng, L.; Su, L.; Yu, X.; Wang, R.; Cui, X.; Tian, H.; Cao, S.; Xia, B. Y.; Shi, J. Electron Redistribution of Ruthenium-Tungsten Oxides Mott-Schottky Heterojunction for Enhanced Hydrogen Evolution. *Appl. Catal., B* **2022**, *308*, 121229.
(48) Zhou, J.; Li, J.; Kan, L.; Zhang, L.; Huang, Q.; Yan, Y.; Chen, Y.; Liu, J.; Li, S.-L.; Lan, Y.-Q. Linking Oxidative and Reductive Clusters to Prepare Crystalline Porous Catalysts for Photocatalytic CO_2 Reduction with H_2O. *Nat. Commun.* **2022**, *13*, 4681.
(49) Zhou, W.; Li, W.; Wang, J.-Q.; Qu, Y.; Yang, Y.; Xie, Y.; Zhang, K.; Wang, L.; Fu, H.; Zhao, D. Ordered Mesoporous Black TiO_2 as Highly Efficient Hydrogen Evolution Photocatalyst. *J. Am. Chem. Soc.* **2014**, *136*, 9280−9283.
(50) Sun, B.; Zhou, W.; Li, H.; Ren, L.; Qiao, P.; Li, W.; Fu, H. Synthesis of Particulate Hierarchical Tandem Heterojunctions toward Optimized Photocatalytic Hydrogen Production. *Adv. Mater.* **2018**, *30*, 1804282.
(51) Zhang, X.; Wang, Y.; Chang, K.; Yang, S.; Liu, H.; Chen, Q.; Xie, Z.; Kuang, Q. Constructing Hollow Porous Pd/H-TiO_2 Photocatalyst for Highly Selective Photocatalytic Oxidation of Methane to Methanol with O_2. *Appl. Catal., B* **2023**, *320*, 121961.
(52) Zhu, W.; Shen, M.; Fan, G.; Yang, A.; Meyer, J. R.; Ou, Y.; Yin, B.; Fortner, J.; Foston, M.; Li, Z.; Zou, Z.; Sadtler, B. Facet-Dependent Enhancement in The Activity of Bismuth Vanadate Microcrystals for The Photocatalytic Conversion of Methane to Methanol. *ACS Appl. Nano Mater.* **2018**, *1*, 6683−6691.
(53) Nosaka, Y.; Nosaka, A. Y. Generation and Detection of Reactive Oxygen Species in Photocatalysis. *Chem. Rev.* **2017**, *117*, 11302−11336.
(54) Alagona, G.; Ghio, C.; Kollman, P.; Bifurcated, Vs. Bifurcated vs. linear hydrogen bonds: dimethyl phosphate and formate anion interactions with water. *J. Am. Chem. Soc.* **1983**, *105*, 5226−5230.
(55) Jiang, S.; Klingan, K.; Pasquini, C.; Dau, H. New Aspects of Operando Raman Spectroscopy Applied to Electrochemical CO_2 Reduction on Cu Foams. *J. Chem. Phys.* **2019**, *150*, 041718.
(56) Zhao, Y.; Zhao, Y.; Waterhouse, G. I. N.; Zheng, L.; Cao, X.; Teng, F.; Wu, L.-Z.; Tung, C.-H.; O'Hare, D.; Zhang, T. Layered-Double-Hydroxide Nanosheets as Efficient Visible-Light-Driven Photocatalysts for Dinitrogen Fixation. *Adv. Mater.* **2017**, *29*, 1703828.
(57) Zeng, Y.; Tang, Z.; Wu, X.; Huang, A.; Luo, X.; Xu, G. Q.; Zhu, Y.; Wang, S. L. Photocatalytic Oxidation of Methane to Methanol by Tungsten Trioxide-Supported Atomic Gold at Room Temperature. *Appl. Catal., B* **2022**, *306*, 120919.
(58) Agarwal, N.; Freakley, S. J.; McVicker, R. U.; Althahban, S. M.; Dimitratos, N.; He, Q.; Morgan, D. J.; Jenkins, R. L.; Willock, D. J.; Taylor, S. H.; Kiely, C. J.; Hutchings, G. J. Aqueous Au-Pd Colloids Catalyze Selective CH_4 Oxidation to CH_3OH with O_2 under Mild Conditions. *Science* **2017**, *358*, 223−227.
(59) Wang, P.; Shi, R.; Zhao, Y.; Li, Z.; Zhao, J.; Zhao, J.; Waterhouse, G. I. N.; Wu, L.-Z.; Zhang, T. Selective Photocatalytic Oxidative Coupling of Methane via Regulating Methyl Intermediates over Metal/ZnO Nanoparticles. *Angew. Chem., Int. Ed.* **2023**, *62*, No. e202304301.
(60) Shang, F.-K.; Li, Y.-H.; Qi, M.-Y.; Tang, Z.-R.; Xu, Y.-J. Photocatalytic Materials for Sustainable Chemistry via Cooperative Photoredox Catalysis. *Catal. Today* **2023**, *410*, 85−101.

Recommended by ACS

Study on the Properties of the Ferroelectric Photocatalytic Hydrogen Evolution Reaction for Chemically Functionalized Phosphorene Nanosheets
Mingyuan Wang, Shuangying Lei, *et al.*
JULY 20, 2023
ACS APPLIED ENERGY MATERIALS
READ

Core–Shell β-SiC@PPCN Heterojunction for Promoting Photo-Thermo Catalytic Hydrogen Production
Dechao Wang, Qiang Liao, *et al.*
JULY 19, 2023
ACS CATALYSIS
READ

Rational Design of Black Phosphorus-Based Direct Z-Scheme Photocatalysts for Overall Water Splitting: The Role of Defects
Yingcai Fan, Mingwen Zhao, *et al.*
OCTOBER 03, 2022
THE JOURNAL OF PHYSICAL CHEMISTRY LETTERS
READ

Hollow Multishell-Structured TiO_2/$MAPbI_3$ Composite Improves Charge Utilization for Visible-Light Photocatalytic Hydrogen Evolution
Wensheng Han, Dan Wang, *et al.*
MARCH 21, 2022
INORGANIC CHEMISTRY
READ

Get More Suggestions >

https://doi.org/10.1021/acsami.3c06376
ACS Appl. Mater. Interfaces 2023, 15, 36280−36288